

Graphical Abstract

Design, Calibration, and Embedded Integration of a Six-Axis Force/Torque Sensor with a Physical Human–Robot Interaction Case Study on a 3-DOF Delta Parallel Robot

Amirhossein Ehsani, Navid Asadi, Mohadeseh Aslani, Mehdi Tale Masouleh, Mohamad Reza Hairi Yazdi, Mohamad Reza Nayeri

Highlights

Design, Calibration, and Embedded Integration of a Six-Axis Force/Torque Sensor with a Physical Human–Robot Interaction Case Study on a 3-DOF Delta Parallel Robot

Amirhossein Ehsani, Navid Asadi, Mohadeseh Aslani, Mehdi Tale Masouleh, Mohamad Reza Hairi Yazdi, Mohamad Reza Nayeri

- Present a compact six-axis strain-gauge F/T sensor with embedded 24-bit synchronized acquisition.
- Develop a low-cost decoupled calibration rig achieving >99.4% accuracy and sub-0.015 N m torque resolution.
- Demonstrate pHRI on a Delta robot with admittance control, virtual walls, and passivity-based Z-width adaptation.

Design, Calibration, and Embedded Integration of a Six-Axis Force/Torque Sensor with a Physical Human–Robot Interaction Case Study on a 3-DOF Delta Parallel Robot

Amirhossein Ehsani

Human and Robot Interaction Laboratory, University of Tehran,

Navid Asadi

Human and Robot Interaction Laboratory, University of Tehran,

Mohadeseh Aslani

Human and Robot Interaction Laboratory, University of Tehran,

Mehdi Tale Masouleh

Human and Robot Interaction Laboratory, University of Tehran,

Mohamad Reza Hairi Yazdi

School of Mechanical Engineering, University of Tehran,

Mohamad Reza Nayeri

School of Electrical Engineering, University of Tehran,

Abstract

This paper presents the design, fabrication, and calibration of a compact six-axis force/torque (F/T) sensor tailored for physical human–robot interaction (pHRI). The mechanical transducer employs a cruciform elastic body instrumented with full-bridge strain gauges and is paired with a custom four-layer PCB featuring a low-noise analog front end, a 24-bit AD7794 ADC, and an STM32 microcontroller for synchronized multi-channel acquisition. An economical calibration rig applies decoupled reference loads along all six axes using repeatable cable–pulley routing and known moment arms. Linear least-squares fitting yields a diagonal calibration map with nonlinearity below 0.39%FS, repeatability within 0.38%FS, and accuracy exceeding 99.4% on all

axes. The force and torque resolutions (99% criterion) are better than 0.47 N and 0.015 N m, respectively. A pHRI case study on a 3-DOF Delta robot demonstrates free-space hand-guidance and interaction with software-defined virtual walls under a discrete-time admittance controller. Energy-based passivity monitoring and Z-width adaptation automatically modulate wall stiffness and damping, ensuring stable, non-energetic contact. The results confirm that the proposed sensor and control pipeline provide reliable, low-latency force feedback suitable for safe, intuitive human–robot cooperation.

Keywords: Six-axis force/torque sensor, Strain gauge, Calibration, Admittance control, Passivity, Physical human–robot interaction (pHRI), Delta robot

1. Introduction

The six-axis force/torque (F/T) sensor is a precise measurement device with the ability to capture forces and moments along the three orthogonal axes— x , y , and z [1]. These sensors are designed to accurately measure multi-axis forces and torques, making them a vital tool for various applications and fields where real-time force and moment data are critical, such as robotics [2, 3], research laboratories [4], aerospace industries [5], industrial machinery [6], and medical applications [7].

In minimally invasive and robot-assisted surgeries, the application of force/torque sensors is increasing to achieve accurate and real-time force feedback. For example, FBG-based six-axis sensors remain operational even after partial structural damage, enabling reliable use in surgery [8]. In orthopedic procedures, a dual F/T sensor system with adjustable admittance control delivers six-DOF feedback while minimizing excessive force during bone alignment [7]. Strain gauges, which are usually present in six-axis F/T sensors, are also embedded in surgical instruments; a case in point is the integration of ultra-thin Nitinol strain sensors into tools for high-sensitivity and compact force measurement [9]. Strain sensors are also essential in robot-assisted heart surgery, in which cardiac motion is accounted for to provide safe and precise control [10].

Beyond medical applications, six-axis F/T sensors are widely deployed in collaborative robotics for safe human–robot interaction and intuitive hand-guiding [3]. Task-oriented designs enhance precision in assembly tasks such as peg-in-hole operations [4], while they also improve force measurement

in industrial automation [11] and aerospace sensing [12]. Min et al. [13] presented a joint torque sensor with high-stiffness and low-crosstalk compact strain gauge topology, which enables accurate moment measurement without compromising arm rigidity.

Within *Mechanism and Machine Theory* (MMT), mechanism-level analyses have directly informed six-axis sensing architectures: Stewart-platform sensors operated near singularity provide mechanical amplification for increased moment sensitivity [14], while hyperstatic, fully pre-stressed designs improve stiffness and accuracy in compact six-axis layouts [15]. Compliant parallel structures have also been modeled in full six-component statics and stiffness, e.g., a 3-RPPS compliant F/T sensor, providing guidance on decoupling and sensitivity distribution [16].

Physical human–robot interaction (pHRI) has emerged as a central research area in robotics and mechatronics, particularly in settings where robots and humans share a common workspace or collaborate in executing tasks. Six-axis F/T sensors play a central role in this effort as they provide precise force feedback and enable flexible control schemes that combine safety and productivity. Existing research underscores the importance of variable admittance control that dynamically varies the compliance of a robot to ensure stable interaction [17]. Adaptive impedance control methods also play a crucial role in adapting to the stochastic dynamics of the human operator, ultimately resulting in better task performance and user safety [18]. Integrating F/T sensors within a parallel robot configuration has further demonstrated promise, as it delivers accurate force data crucial for direct human engagement [19].

Complementing these, MMT has reported foundational pHRI contributions: an influential “atlas” frames safety and dependability aspects of physical interaction [20]; task-oriented HRI control was developed for haptic master manipulators in surgical settings [21]; force-estimating compliant grippers were explored for direct human–limb manipulation [22]; and external-force self-sensing strategies were proposed for backdrivable cable–pulley surgical manipulators, integrating model-based and estimator components for robust tracking [23].

This paper focuses on a sensor design that is based on strain gauge technology to convert mechanical deformation into measurable electrical signals. Strain gauges are accurate, small, and easily configured to measure multidimensional strains. They are, however, difficult to bond and require careful overload protection. The range of signals produced is in the millivolt

range; therefore, careful shielding and amplification are required. By mounting these strain gauges on a structure and using a suitable amplification through a Wheatstone bridge circuit, it is possible to measure this voltage [24, 25]. Early studies by Sharifzadeh et al. [19] and Ballo et al. [26] demonstrated the potential of strain-gauge-based sensors but revealed challenges in calibration accuracy and fabrication complexity. Alternatives such as fiber Bragg grating (FBG) sensors were later introduced to improve sensitivity and fault tolerance [8]. To address signal quality issues, Haddab et al. [27] applied Kalman filtering with strain gauges to enhance dynamic force measurements under noisy conditions. Denkena et al. [28] investigated robust sensor integration, embedding strain gauges into hydraulic clamping systems with FEM-guided placement and structural optimization. Other approaches, including novel sensor configurations and multi-objective optimization strategies, have further advanced measurement reliability.

Broader surveys consolidate multi-axis sensing technologies, elastic-body topologies, and error sources relevant to reliable pHRI [29]. HRI-oriented multi-axis sensing for rehabilitation further underscores ergonomics and robustness in human contact scenarios [30]. Because installation and thermal conditions often shift calibration matrices, model-based *in situ* approaches and temperature-compensated procedures avoid dismounting and improve long-term accuracy on humanoids and floating-base systems [31, 32]. Architecturally, classic isotropic designs and wrist-type transducers remain influential for compact end-effector integration [33, 34], while flexure-based six-DoF transducers and inductive-resonance methods offer repeatable, compact alternatives with high sensitivity [35, 36].

Building on previous advancements and the work presented in [25], where an optimized six-axis F/T sensor was introduced using a genetic-algorithm-based multi-objective approach to refine structural dimensions and strain gauge placements, several key improvements are proposed in this study. A review of existing work, for example that of Lin et al. [37], reveals that while their designs achieved strong structural optimization, they lacked a dedicated calibration mechanism for minimizing systematic errors. The objective of this work is to enhance the performance of a six-axis F/T sensor by introducing an improved calibration setup—developed and refined through rigorous design iterations—to provide higher precision and repeatability. The setup significantly reduces measurement variability, providing a sound foundation for accurate force/torque estimation and robust pHRI experiments.

This paper first provides an overview of the sensor system design and

development in Section 2. Section 3 details the sensor calibration procedure and the data processing methodology. Section 4 reports the resulting performance indices and compares the custom sensor with existing commercial and research devices. In Section 5, a case study involving physical human–robot interaction using a Delta robot is presented. Finally, Section 6 concludes the paper and outlines future research paths.

Nomenclature

F_x, F_y, F_z	Cartesian force components [N]
M_x, M_y, M_z	Cartesian torque components [N m]
$\mathbf{c} \in \mathbb{R}^6$	Vector of ADC output counts (sensor channels) [count]
$S \in \mathbb{R}^{3 \times 6}$	Calibration matrix mapping counts to forces [N/count]
$\mathbf{b} \in \mathbb{R}^3$	Calibration offset vector [N]
M	Virtual inertia matrix in admittance model
B	Virtual damping matrix
K_c	Centering stiffness matrix
K_w, D_w	Virtual wall stiffness and damping
$\mathbf{p} = [x \ y \ z]^\top$	End-effector position in base frame [m]
\mathbf{v}	End-effector Cartesian velocity [m/s]
\mathbf{a}	End-effector Cartesian acceleration [m/s ²]
\mathbf{n}	Outward unit normal of virtual wall [-]
\mathbf{p}_w	Point on virtual wall plane [m]
p_{pen}	Penetration depth into virtual wall [m]
v_n	Normal component of end-effector velocity [m/s]
τ	Deadband threshold on interaction force [N]
α	IIR low-pass smoothing factor (here $\alpha = 0.28$) [-]
Δt	Control and integration time step [s]
γ_p	D-floor gain for passivity-enforcing damping [-]
P_{env}	Power at environment (wall) port [W]
E_{env}	Stored environment energy in the tank [J]
λ	Leakage factor of energy tank (here $\lambda = 0.985$) [-]
K_{\min}, K_{\max}	Lower/upper bounds on wall stiffness
η_\downarrow	Stiffness decay factor in Z-width adaptation [-]
r_\uparrow	Stiffness growth rate in Z-width adaptation
FS	Full-scale range of the corresponding channel

2. Sensor System Design and Development

The six-axis force/torque sensor developed in this study is the result of detailed theoretical modeling and practical engineering design. This section provides a comprehensive overview of the sensor's design, including its mechanical layout, signal conditioning electronics, and the firmware running on its embedded microcontroller. As shown in Figure 1 and based on the original structure introduced by Ehsani et al. [25], the present version incorporates several key upgrades aimed at enhancing accuracy, durability, and ease of manufacturing.

Theoretically, the design is rooted in solid mechanics, and Timoshenko beam theory is used to forecast how the structure will strain under external forces. This is paired with signal processing methods to measure and separate the different force and torque components precisely.

On the practical side, sensor construction benefits from appropriate material selection, precision manufacturing techniques such as wire electrical discharge machining (EDM), and a custom-built printed circuit board (PCB) equipped with a 24-bit analog-to-digital converter (ADC) for real-time data collection. These updates together lead to better resolution, more consistent performance, and simpler integration. They also pave the way for advanced calibration and signal processing methods.

2.1. Mechanical Structure and Sensing Mechanism

The sensor's mechanical structure is a cruciform layout composed of four flexible beams arranged in a symmetrical cross. This design, inspired by proven decoupled configurations [38, 39], plays a key role in providing high sensitivity while minimizing interference between different force and torque readings. The main elastic body, which converts external mechanical forces into measurable strain, is machined from T6-7075 aluminium alloy. This material was chosen for its excellent strength-to-weight ratio, stiffness, and fatigue resistance. Additional structural parts, such as the top and bottom plates and vertical supports, are made of T6-6061 aluminium alloy, which offers a good balance of durability, cost-effectiveness, and ease of manufacturing.

The sensor uses 16 dual-element strain gauges (32 single elements) that are carefully mounted on the beams. Their exact positions were determined using detailed finite element analysis and genetic optimization to ensure they are placed where the beams experience the most consistent and strongest strain under load. Each gauge sits 5 mm from where the elastic zone of the

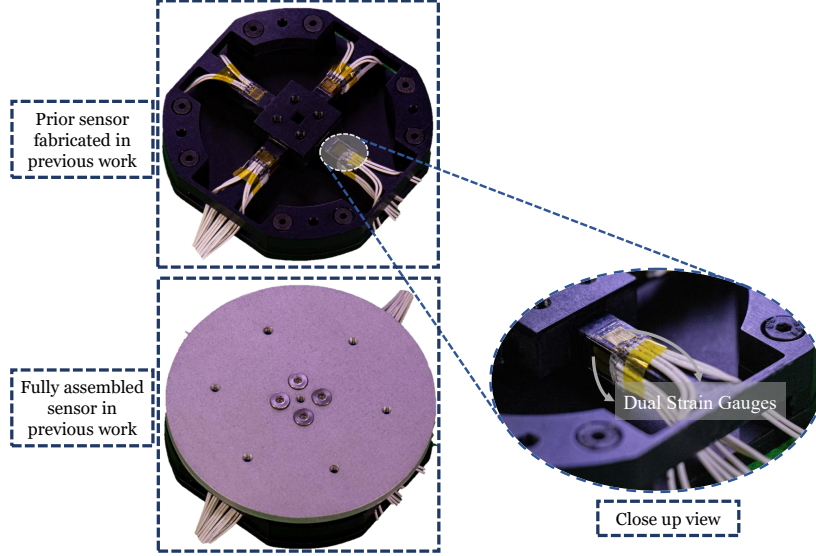


Figure 1: Prior six-axis force–torque sensor from [25]: internal structure and fully assembled unit, with a close-up showing dual strain gauges bonded on each sensing beam. This prototype formed the basis for the improved sensor presented in this study.

beam begins, a spot identified as ideal for maximizing accuracy while avoiding issues like nonlinear distortion or strain overlap.

Due to the symmetrical structure and strategic gauge placement, signals from the strain gauges are processed through six separate Wheatstone bridge circuits, each dedicated to one of the force or torque axes ($F_x, F_y, F_z, M_x, M_y, M_z$). These circuits are naturally balanced when the sensor is at rest, giving a stable baseline. Using full-bridge setups also improves resistance to electrical noise, increases sensitivity, and provides more linear readings.

As shown in Figure 2 and based on the previous prototype of Ehsani et al., the present version keeps the original mechanical design but introduces a fully customized circuit board for data collection and signal processing. This board replaces the older modular HX-711 system with an advanced design that includes a low-noise analog front-end, a 24-bit ADC (AD7794-BRUZ), anti-aliasing filters, and SPI communication with the microcontroller. These upgrades deliver higher resolution, faster sampling, lower noise, and better synchronization between channels. This new hardware setup marks the most significant improvement in design, allowing for more precise calibration, real-time performance gains, and broader use in robotics applications.

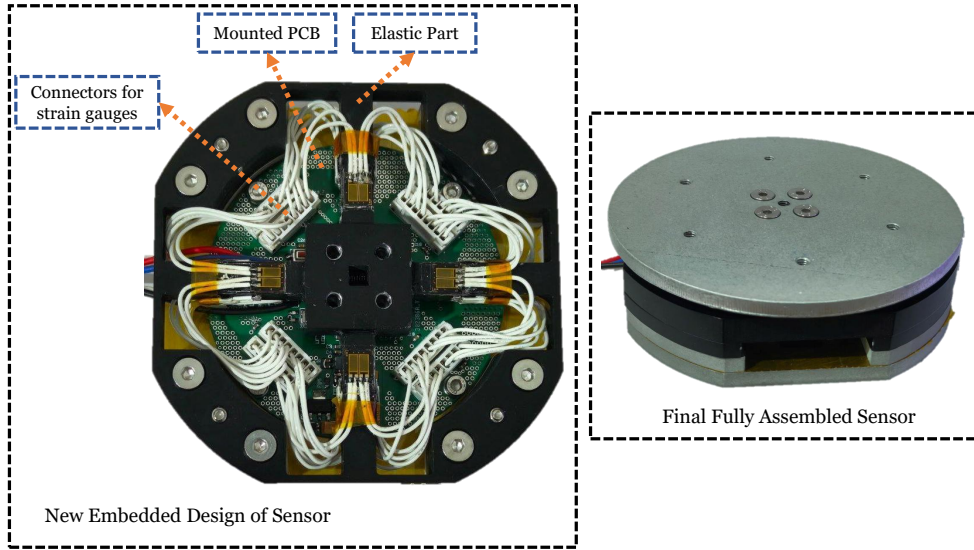


Figure 2: New embedded six-axis force–torque sensor featuring an integrated PCB for strain-gauge connection and low-noise signal conditioning. The embedded layout enhances wiring symmetry and reduces electromagnetic interference.

2.2. Electronic Architecture and Signal Acquisition

The sensor design is founded upon six full-bridge Wheatstone circuits that convert mechanical strain into a differential voltage. External force- or torque-induced resistance changes in the strain gauges unbalance all six bridges, producing low-level analog signals proportional to the external load. To make them appropriate for multi-axis force/torque measurement, these signals need to be stabilized, amplified, and converted into digital form with low noise. A layout diagram of the PCB is shown in Figure 2, and the overall signal flow is depicted in the block diagram in Figure 3.

The digital voltage (DVDD) for the STM32 microcontroller and for the AD7794 ADC is provided from a regulated 3.3 V supply, which is derived from a low-dropout regulator. At the same time, a precision 2.5 V reference (ADR391AUJZ) with high accuracy is buffered through a transistor stage to give stable excitation for the six bridges while delivering the required drive current without sag in voltage. This arrangement gives equal excitation to the six bridges, lowers drift during calibration, and enhances long-term conversion stability. The circuit is built on a four-layer PCB to minimize routing noise and digital–analog coupling. The sensing chain centers around the AD7794, a 24-bit sigma–delta analog-to-digital converter optimized for

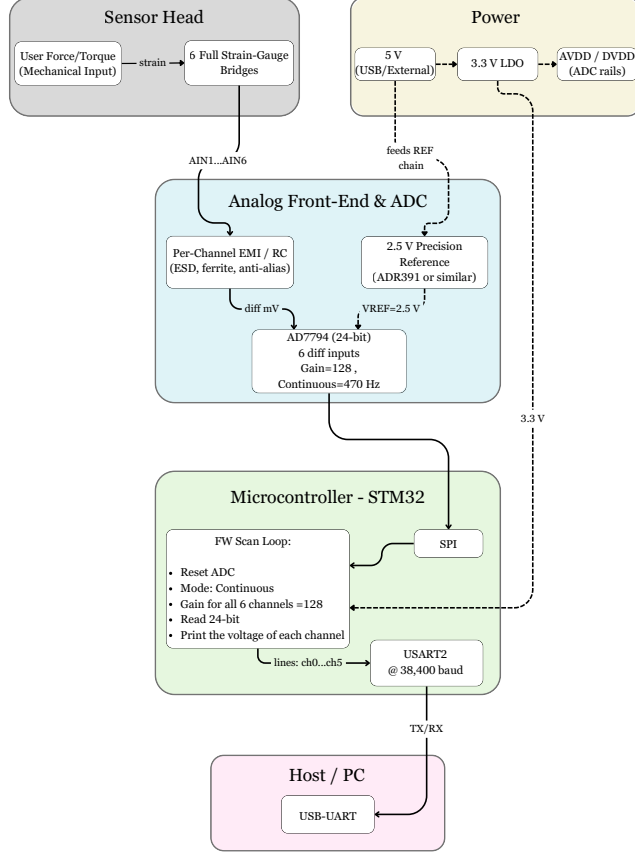


Figure 3: Block diagram of the acquisition chain showing the path from strain-gauge bridges to the host PC. Mechanical strain is first converted into differential voltages and conditioned by filtering and a precision 2.5 V reference before 24-bit digitization in the AD7794. Channel sequencing and SPI data transfer are managed by an STM32 microcontroller, transmitting results over UART to the host for real-time display.

bridge measurements.

The ADC operates in continuous-conversion mode at 470 Hz to deliver high-resolution, low-latency updates. The six channels are sequentially scanned, with the reference input tied to the 2.5 V excitation for ratiometric conversion. Both analog and digital filtering methods are utilized to reject noise: local decoupling capacitors reject high-frequency switching noise, RC filters reject low-frequency interference, and the on-chip digital ADC filter rejects line-frequency interference. An STM32F0 microcontroller controls data acqui-

sition, switches channels, and reads data quickly. A number of firmware-level optimizations are implemented in order to achieve peak throughput, such as direct polling of the ADC ready flag, rapid reconfiguration of the channel registers, and low-overhead formatting methods for transmission.

With these optimizations, all six channels can be scanned within approximately 44 ms, corresponding to an effective sampling rate of about 22 Hz per channel. This rate provides sufficient temporal resolution for quasi-static calibration tests and physical human–robot interaction testing. Processed data are transmitted over UART for real-time viewing and logging, and USB is also supported as a redundancy interface. The combination of meticulous voltage regulation, stable bridge excitation, high-resolution conversion, extensive filtering, four-layer PCB manufacturing, and optimized firmware provides a robust and reliable electronic platform for six-axis force/torque sensing.

3. Calibration Setup and Methodology

3.1. Sensor Calibration and Performance Evaluation

Experimental calibration is a vital process to establish a reliable correlation between the mechanical loads applied and the electrical outputs of a force/torque sensor. Correct calibration eliminates systematic errors caused by structural tolerances, misalignments, and signal drift and therefore yields a reliable multi-axis measurement. Our conceptual design for the calibration setup was inspired by the work of Lin et al. [37], who designed a novel mechanically fully decoupled six-axis force/torque sensor and a purpose-specific calibration test-bed. They employed accurate loads through a sequence of rigid linkages and constraint devices that decoupled each degree of freedom so that individual forces and torques could be applied independently without cross-coupling other axes. This decoupled approach considerably simplified the computation of the calibration matrix and improved the accuracy of computed sensitivities. However, their implementation required close manufacturing tolerances, complex multi-piece assembly, and costly machining, and so was less suited to quick prototyping or small-lot laboratory use. In the present design, the conceptual idea of employing highly controlled, axis-specific loads was retained but the mechanical design was re-arranged for fewer parts, reduced fabrication cost, and simpler alignment without loss of accuracy sufficient for six-axis calibration.

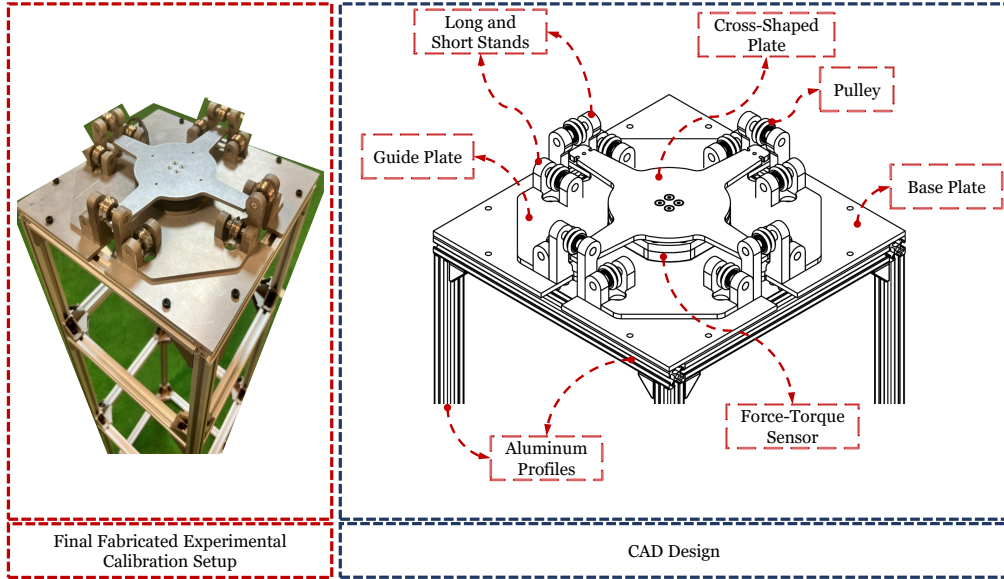


Figure 4: Calibration test-bed: CAD design (right) and fabricated setup (left). A cross-shaped loading plate distributes cable forces while promoting decoupling between measurement axes. Low-friction pulleys route the cables so that reference loads act normal to, and are aligned with, the selected axis. A precision guide plate locates the bearing-supported stands; interchangeable long and short stands accommodate lateral versus axial loading and positive/negative directions. The six-axis force-torque sensor is rigidly clamped at the center, and the assembly is fixed to a base plate mounted on aluminum profiles that elevate the rig and provide clearance for the ropes and hanging weights used during calibration.

3.1.1. Calibration Test-bed and Loading Procedures

The mechanical calibration system designed in this study is shown in Figure 4. It is constructed upon a stiff aluminum-profile frame that supports three main plates: a base plate, a mid-level guide plate, and a cross-shaped top plate. The base plate provides the primary mounting surface, the guide plate precisely positions the bearing-supported shafts and pulleys, and the cross-shaped plate evenly spreads the cable-driven loads applied to the sensor interface. Short and tall machined aluminum supports position the precision steel shafts supporting the pulleys and define the vertical spacing needed for cable routing.

Certain design enhancements were made to overcome the bulkiness, costliness, and space inefficiency encountered in Lin's design. Wire-cut manufacturing substituted heavy CNC machining to produce lightweight, high-precision aluminum plates at reduced cost and assembly complexity. Guide plate

geometry was optimized for reduced material usage and weight, which also simplified aligning the support legs. The steel shafts were designed with a stepped shape to be easily centered with pulleys and to prevent axial drift under load, and smooth operation was maintained through double ball bearings. Pulley brackets were tightened in a cinching configuration around the loading zone, maintaining minimal cable length in order to reduce compliance and hysteresis, and clearance tracks were built in for the free flow of cables.

Reference loads are applied through calibrated weights suspended from semi-static cords passed over low-friction V-groove pulleys. To supply torque generation, moment-arm lengths of known value are incorporated in the cable path, whereby pure torques around desired sensor axes can be introduced. The layout allows for precise and reproducible application of forces and torques in all six directions in a compact, modular, and accessible format.

3.1.2. Calibration Model Derivation and Validation

To establish the quantitative relationship between the sensor outputs and the reference loads, a linear calibration model was applied. Each of the six physical components ($F_x, F_y, F_z, M_x, M_y, M_z$) is mapped to one of the six sensor output channels ($ch_0 \dots ch_5$) by an affine model of the following form:

$$F = a \cdot ch + b \quad (1)$$

where F is the applied force or torque, ch is the raw sensor voltage measurement, and a and b are the gain and offset terms, respectively. The coefficients were found by applying the least-squares method. For N sets of calibration data (F_i, ch_i), the approach minimizes the squared residual error:

$$E = \sum_{i=1}^N (F_i - (a \cdot ch_i + b))^2 \quad (2)$$

leading to the closed-form solutions:

$$a = \frac{N \sum ch_i F_i - \sum ch_i \sum F_i}{N \sum (ch_i)^2 - (\sum ch_i)^2}, \quad b = \frac{\sum F_i - a \sum ch_i}{N}. \quad (3)$$

This procedure was used independently for each of the six channels in order to provide a diagonal calibration matrix that maps ($ch_0 \dots ch_5$) to ($F_x, F_y, F_z, M_x, M_y, M_z$).

Calibration reference loads were manufactured from specially prepared hollow 3D-printed masses filled with metal washers and screws to create well-defined target masses. Their ultimate mass was verified by a digital balance of 0.01 g resolution for accurate force estimation. Weights were mounted on the test-bed with low-stretch semi-static cords wrapped around ball-bearing pulleys in order to provide low frictional losses and minimize off-axis forces.

Data were collected for each axis separately by suspending the calibrated weights to apply known forces or torques along or about the three Cartesian axes. Forces along x and y were applied using slots on the cross-shaped plate, while F_z was generated by vertical loading through pulleys. Bending torques (M_x, M_y) were induced by applying upward and downward forces at opposite edges, and torsional torque M_z was applied via a pair of opposing lateral forces. Each loading condition was repeated three times to improve statistical reliability.

A custom graphical user interface (GUI) in Python using PyQt5 was developed to streamline the calibration process. The GUI provides real-time plotting of all six channels, taring via mean subtraction of the following 20 samples, consecutive sampling of 500 samples in every step load, and real-time low-pass filtering with a first-order exponential IIR filter with a user-variable smoothing factor α . The parameter α controls the trade-off between response and smoothness of the filtered signal, with smaller values yielding heavier smoothing and larger values yielding faster reaction to transients. The discrete-time implementation of a first-order low-pass filter is as follows:

$$y[n] = \alpha x[n] + (1 - \alpha)y[n - 1] \quad (4)$$

where $x[n]$ is the input signal, $y[n]$ is the output signal, and α is the smoothing factor as defined in (4). In the experiments and in the PHRI controller implementation, a value of $\alpha = 0.28$ was selected by manual tuning to balance noise suppression and responsiveness. The software determines the least-squares calibration coefficients for every channel upon acquisition, stores them in binary calibration files, and utilizes them to correct arriving data in real time. The GUI also includes the ability to plot calibration curves, including the measured data points and best-fit lines for inspection.

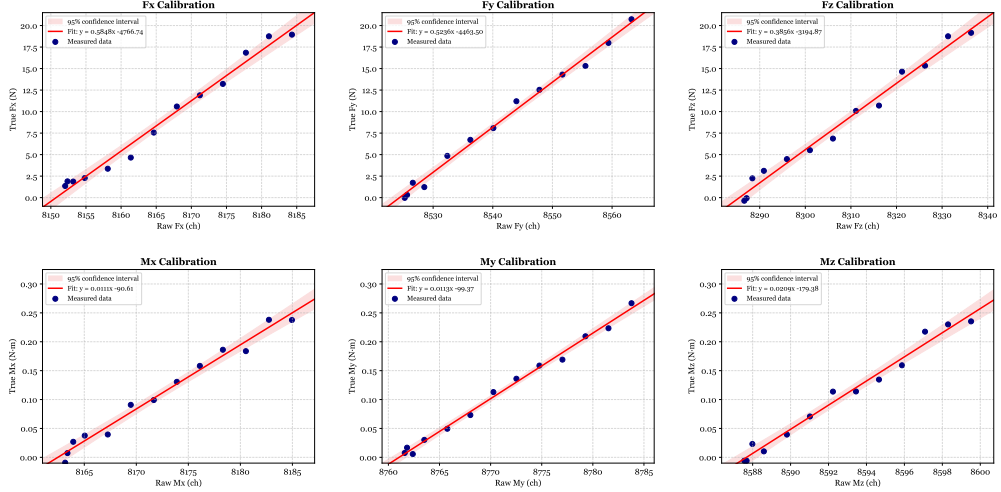


Figure 5: Comprehensive calibration results for all six force and torque channels of the custom six-axis F/T sensor. The red lines indicate the fitted linear calibration models with shaded regions representing 95% confidence intervals.

4. Results

To quantitatively assess the performance of the developed six-axis F/T sensor, a comprehensive calibration campaign was performed for all six force and torque components. The extracted performance indices—sensitivity, offset, nonlinearity, resolution, repeatability, precision, hysteresis, and accuracy—are summarized in Table 1. Presenting these indices in a consolidated form avoids repetition in the main text while enabling direct comparison across axes.

The obtained indices confirm that the sensor behaves linearly and consistently across its entire operating range. The full-scale capacity of the force channels exceeds 200 N, making the measured sub-newton resolution particularly noteworthy for a strain-gauge-based design. Despite the relatively low-cost hardware and compact form factor, the accuracy exceeds 99.4% for all axes, placing the device close to the performance envelope of industrial-grade units.

Repeatability, precision, and hysteresis all remain within narrow limits, indicating stable deformation characteristics of the cruciform structure and effective noise rejection in the analog front end. Since all numerical details are contained in Table 1, the text focuses on qualitative interpretation.

To contextualize the performance, Table 2 compares the proposed sensor

Table 1: Performance indices of the proposed six-axis F/T sensor for each axis. All values are directly obtained from repeated calibration trials.

Index	Fx	Fy	Fz	Mx	My	Mz	Unit
Sensitivity	0.6103	0.5182	-0.3961	0.0113	-0.0111	-0.0206	N, N m/count
Offset (%FS)	0.0289	-0.1201	-0.0368	0.0562	0.0670	0.0414	%FS
Nonlinearity	0.3285	0.3860	0.2355	0.2400	0.0295	0.0215	%FS
Resolution (99%)	0.4690	0.4700	0.3760	0.0148	0.0078	0.0117	N, N m
Repeatability	0.1938	0.3790	0.3164	0.0162	0.0103	0.0072	%FS
Precision	0.2741	0.5360	0.4474	0.0229	0.0146	0.0102	%FS
Hysteresis	0.0917	0.0408	0.0510	0.1881	0.0470	0.0940	%FS
Accuracy	99.551	99.453	99.677	99.732	99.856	99.843	%

Table 2: Comparison of the proposed six-axis F/T sensor with representative commercial and research devices. Only figures explicitly reported in this work or cited references are included.

Sensor	Nonlinearity / AAE	Resolution (force / torque)	Remarks
Proposed sensor (this work)	< 0.39%FS	< 0.47 N, < 0.015 N m	200 N full-scale range; embedded 24-bit ADC; compact and low-cost design
ATI Axia80 (industrial)	Not reported here	0.1 N, 0.005 N m	Higher resolution but substantially higher cost and electronic complexity
Lin et al. [37]	AAE 1.25–2.37%	Not reported here	Fully decoupled elastic structure; multi-component calibration testbed

with representative devices from both the commercial and research literature. Only metrics explicitly reported in this study or in the cited works are included.

As shown in Table 2, the proposed sensor exhibits lower nonlinearity than the decoupled design of Lin et al. and achieves a resolution close to that of the ATI Axia80 despite its simpler and lower-cost hardware. Given its 200 N full-scale range, the sub-newton resolution is highly suitable for pHRI applications, where interaction forces typically remain below 15 N.

Figure 5 shows representative calibration curves for all six channels. The data points lie tightly along the fitted regression lines, indicating low noise and good repeatability. Minor differences between the plotted slopes and those in Table 1 arise because the figure displays a single raw trial, whereas the table summarizes averaged results from multiple filtered runs. .

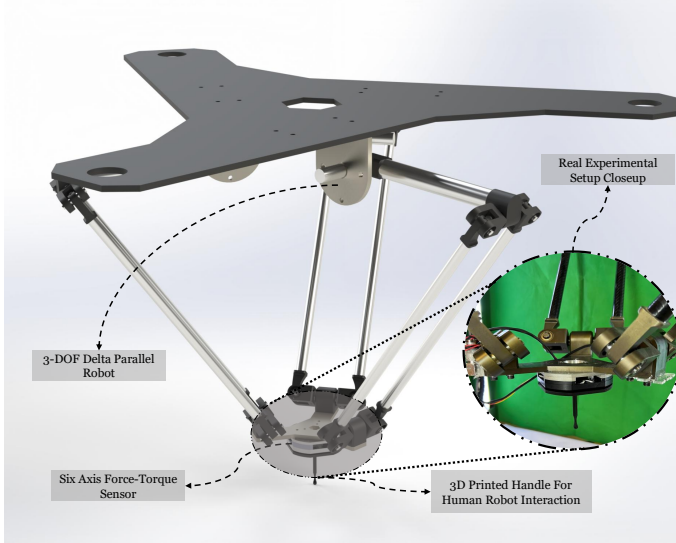


Figure 6: pHRI platform: 3-DOF Delta robot with the custom six-axis F/T sensor and ergonomic handle. Virtual walls are defined as planes in the base frame $\{\mathcal{B}\}$.

5. Case Study: PHRI with Delta Robot

This section reports a complete physical human–robot interaction (pHRI) case study on a 3-DOF Delta robot equipped with the custom six-axis F/T sensor described earlier. We formalize the sensing and control pipeline, derive the discrete-time admittance law with virtual fixtures, and present passivity-based stabilization and Z-width adaptation. The experiments focus on free-space hand-guidance and “virtual wall” interactions, which are representative for safe, intuitive pHRI on translational parallel robots [19, 17, 18].

5.1. Experimental platform and coordinate frames

The Delta mechanism provides pure translation $\mathbf{p} = [x \ y \ z]^\top$ of the end-effector in the base frame $\{\mathcal{B}\}$. The F/T sensor is mounted coaxially between the moving platform and the human handle; its calibrated outputs are aligned with $\{\mathcal{B}\}$ so that the measured interaction force is $\mathbf{F}_s = [F_x \ F_y \ F_z]^\top$. Moments are monitored for safety but not used for control. A microcontroller acquires the six bridge channels, performs SPI transfer from the 24-bit ADC, and streams data to the host PC; the PC runs the pHRI loop and sends Cartesian velocity (or small position) commands to the three drives via the robot controller. Inverse kinematics $\boldsymbol{\theta} = \text{IK}(\mathbf{p})$ and the (analytical) inverse Jacobian $\dot{\boldsymbol{\theta}} = J^{-1}(\boldsymbol{\theta})\dot{\mathbf{p}}$ provide the interface to joint space.

5.2. Sensor signal conditioning

Let $\mathbf{c} \in \mathbb{R}^6$ denote the vector of ADC counts from the six strain-gauge bridges. The corresponding force estimate is obtained through an affine calibration model

$$\mathbf{F}_{\text{raw}} = S \mathbf{c} + \mathbf{b}, \quad S \in \mathbb{R}^{3 \times 6}, \mathbf{b} \in \mathbb{R}^3, \quad (5)$$

where the matrix S and offset vector \mathbf{b} are determined via least-squares fitting.

During real-time operation, three preprocessing steps are applied:

(i) subtraction of a continuously updated tare bias, (ii) first-order IIR low-pass filtering, and (iii) a deadband to suppress micro-motions near zero force.

These steps are expressed as

$$\tilde{\mathbf{F}}_k = \mathbf{F}_{\text{raw},k} - \bar{\mathbf{F}}_{\text{tare}}, \quad (6a)$$

$$\mathbf{F}_k = \alpha \tilde{\mathbf{F}}_k + (1 - \alpha) \mathbf{F}_{k-1}, \quad (6b)$$

$$\mathbf{F}_{u,k} = \begin{cases} \mathbf{F}_k, & \|\mathbf{F}_k\| \geq \tau, \\ \mathbf{0}, & \text{otherwise.} \end{cases} \quad (6c)$$

A smoothing factor of $\alpha = 0.28$ is used throughout the experiments, providing a balance between responsiveness and noise attenuation, while the deadband threshold is set to $\tau = 2.0$ N to suppress small unintentional motions and sensor drift.

5.3. Admittance control with centering impedance

To generate compliant motion in a velocity-controlled Delta robot, an admittance formulation is employed and augmented with a weak centering spring. The governing relation is

$$M \dot{\mathbf{v}} = \mathbf{F}_u + \mathbf{F}_{\text{wall}} + \mathbf{F}_{\text{cent}} - B \mathbf{v}, \quad \mathbf{F}_{\text{cent}} = -K_c (\mathbf{p} - \mathbf{p}_0), \quad (7)$$

where \mathbf{p} and \mathbf{v} are the end-effector position and velocity, and M , B , and K_c denote the virtual inertia, damping, and centering stiffness matrices. The user-applied force \mathbf{F}_u drives the motion, whereas the virtual wall force \mathbf{F}_{wall} always opposes penetration into a constraint surface. A positive-definite damping matrix B ensures that the dissipation term $B \mathbf{v}$ contributes to the passivity of the overall interaction.

The discrete-time implementation uses a semi-implicit Euler step:

$$\begin{aligned}\mathbf{a}_k &= M^{-1}(\mathbf{F}_{\text{u},k} + \mathbf{F}_{\text{wall},k} + \mathbf{F}_{\text{cent},k} - B \mathbf{v}_k), \\ \mathbf{v}_{k+1} &= \mathbf{v}_k + \Delta t \mathbf{a}_k, \\ \mathbf{p}_{k+1} &= \mathbf{p}_k + \Delta t \mathbf{v}_{k+1},\end{aligned}\tag{8}$$

which provides numerical stability and smooth trajectories suitable for real-time physical human–robot interaction.

5.4. Virtual walls as unilateral spring–damper constraints

A virtual wall is modelled as a unilateral constraint that reacts only when the end-effector attempts to penetrate the boundary. Let the wall be described by the half-space

$$\{ \mathbf{p} \mid \mathbf{n}^\top (\mathbf{p} - \mathbf{p}_w) \leq 0 \},$$

where \mathbf{n} is the outward unit normal and \mathbf{p}_w is any point on the wall. The normal penetration depth and normal velocity are given by

$$p_{\text{pen}} = [\mathbf{n}^\top (\mathbf{p} - \mathbf{p}_w)]_+, \quad v_n = \mathbf{n}^\top \mathbf{v},\tag{9}$$

where $[\cdot]_+$ denotes the positive part, ensuring that forces are generated only during penetration.

The wall exerts a penalty force composed of a linear spring and a viscous damper,

$$\mathbf{F}_{\text{wall}} = -(K_w p_{\text{pen}} + D_w v_n) \mathbf{n}, \quad K_w \geq 0, D_w \geq 0,\tag{10}$$

which pushes the end-effector back into the admissible region. Only the motion perpendicular to the wall is constrained by this model; tangential motion remains unaffected, and no frictional or shear interaction is introduced. This formulation provides a simple and robust mechanism for enforcing unilateral geometric constraints while maintaining smooth user interaction.

5.5. Passivity enforcement and Z-width adaptation

The virtual wall model is complemented by a passivity layer that regulates damping and stiffness to ensure stable interaction under discrete-time implementation. The structure follows standard passivity-based approaches for virtual environments and is tailored to the pHRI sampling rates used in the experiments.

D-floor:: A minimum wall damping level is enforced to guarantee energy dissipation, particularly when the virtual stiffness becomes large. The damping is bounded below by

$$D_w \leftarrow \max(D_w, \gamma_p K_w \Delta t), \quad (11)$$

where $\gamma_p > 0$ is a proportionality gain. In the experiments, a value of $\gamma_p = 1.2$ was used, which provides sufficient damping to counteract discrete-time effects while preserving transparency during light contact.

Passivity observer:: The instantaneous power exchanged at the environment port is

$$P_{\text{env},k} = -\mathbf{F}_{\text{wall},k}^\top \mathbf{v}_k, \quad (12)$$

and the accumulated energy is tracked with a leaky integration,

$$E_{\text{env},k+1} = \lambda E_{\text{env},k} + \max(0, P_{\text{env},k}) \Delta t. \quad (13)$$

The leakage factor $\lambda \in (0, 1)$ prevents long-term drift and keeps the stored energy bounded during extended interaction. A value of $\lambda = 0.985$ was used, corresponding to a gradual decay of accumulated energy over several hundred control cycles.

Z-width adaptation:: The virtual wall stiffness is adapted based on the observed environment energy. When the accumulated energy exceeds a threshold E_{th} , the stiffness is reduced multiplicatively; otherwise, it recovers gradually:

$$K_{w,k+1} = \begin{cases} \max(K_{\min}, \eta_\downarrow K_{w,k}), & E_{\text{env},k} > E_{\text{th}}, \\ \min(K_{\max}, K_{w,k} + r_\uparrow \Delta t), & \text{otherwise.} \end{cases} \quad (14)$$

For the experiments, the parameters were chosen as $K_{\min} = 5 \times 10^{-4}$, $K_{\max} = 0.10$, $\eta_\downarrow = 0.5$, and $r_\uparrow = 0.010$. This configuration yields rapid stiffness reduction during energetic transients, improving stability, followed by a slower, smooth recovery once contact forces diminish.

5.6. Complete PHRI loop (algorithm)

Algorithm 1 Summarized PHRI loop (admittance + virtual walls + passivity + Z-width)

Require: M, B, K_c , wall params (K_w, D_w, γ_p) , tank params $(\lambda, E_{th}, K_{min}, K_{max}, \eta_\downarrow, r_\uparrow)$

Require: Sample time Δt , workspace \mathcal{W} , deadband τ , filter gain α

- 1: Initialize $\mathbf{p}, \mathbf{v}, E_{env} \leftarrow 0$, tare bias $\bar{\mathbf{F}}_{tare}$, last force \mathbf{F}_{-1}
- 2: **while** control active **do**
- 3: Read ADC \mathbf{c} ; compute $\mathbf{F}_{raw} = S\mathbf{c} + \mathbf{b}$
- 4: $\tilde{\mathbf{F}} = \mathbf{F}_{raw} - \bar{\mathbf{F}}_{tare}$ ▷ tare
- 5: $\mathbf{F} = \alpha \tilde{\mathbf{F}} + (1 - \alpha) \mathbf{F}_{-1}$ ▷ low-pass
- 6: $\mathbf{F}_u = \mathbf{F}$ if $\|\mathbf{F}\| \geq \tau$, else $\mathbf{0}$ ▷ deadband
- 7: $\mathbf{F}_{cent} = -K_c(\mathbf{p} - \mathbf{p}_0)$
- 8: $\mathbf{F}_{wall} \leftarrow \mathbf{0}$
- 9: **for all** walls i with $(\mathbf{n}_i, \mathbf{p}_{w,i})$ **do**
- 10: $p_{pen} = \max(0, \mathbf{n}_i^\top (\mathbf{p} - \mathbf{p}_{w,i}))$
- 11: **if** $p_{pen} > 0$ **then**
- 12: $D_w \leftarrow \max(D_w, \gamma_p K_w \Delta t)$ ▷ D-floor
- 13: $v_n = \mathbf{n}_i^\top \mathbf{v}$
- 14: $\mathbf{F}_{wall} -= (K_w p_{pen} + D_w v_n) \mathbf{n}_i$
- 15: **end if**
- 16: **end for**
- 17: $\mathbf{a} = M^{-1}(\mathbf{F}_u + \mathbf{F}_{wall} + \mathbf{F}_{cent} - B\mathbf{v})$
- 18: $\mathbf{v} \leftarrow \mathbf{v} + \Delta t \mathbf{a}$; $\mathbf{p} \leftarrow \text{clamp}_{\mathcal{W}}(\mathbf{p} + \Delta t \mathbf{v})$
- 19: $P_{env} = -\mathbf{F}_{wall}^\top \mathbf{v}$; $E_{env} \leftarrow \lambda E_{env} + \max(0, P_{env}) \Delta t$
- 20: **if** $E_{env} > E_{th}$ **then**
- 21: $K_w \leftarrow \max(K_{min}, \eta_\downarrow K_w)$ ▷ reduce stiffness
- 22: **else**
- 23: $K_w \leftarrow \min(K_{max}, K_w + r_\uparrow \Delta t)$ ▷ recover stiffness
- 24: **end if**
- 25: Send \mathbf{v} (or $\Delta \mathbf{p}$) to robot controller
- 26: $\mathbf{F}_{-1} \leftarrow \mathbf{F}$
- 27: **end while**

5.7. Experimental setup and procedure

Figure 7 summarizes the complete pHRI platform used in the experiments. A 3-DOF Delta robot provides translational motion, and the operator interacts through a 3D-printed handle mounted on the custom six-axis F/T sensor. The sensor's embedded electronics perform strain-gauge conditioning and 24-bit acquisition, and the host PC converts the raw ADC data into forces using tare removal, low-pass filtering, and a deadband.

The processed force drives an admittance controller that combines user input, a centering spring, and unilateral virtual-wall forces. Passivity is maintained by enforcing a minimum wall damping (D-floor) and by monitoring environment energy through a leaky passivity observer. A Z-width adaptation mechanism adjusts the virtual wall stiffness, reducing it during energetic contacts and recovering it smoothly during free motion.

The resulting Cartesian velocities (or position increments) are mapped to joint space via inverse kinematics and executed by the robot's velocity loops. Two tasks were evaluated: free-space hand-guidance and interaction with a planar virtual wall.

5.8. Kinematic response and motion tracking

The filtered Cartesian velocities follow the admittance model predictions closely. During wall contact, the velocity component normal to the wall drops sharply while tangential components remain smooth, confirming that the unilateral constraint correctly suppresses penetration but allows lateral sliding. This transition is achieved without oscillations, validating the adequacy of the damping matrix B and the implemented semi-implicit Euler integration.

5.9. Interaction forces and consistency verification

Force readings from the six-axis sensor show peak contact forces below 8 N, within safe human–robot limits. The derived forces from moment components (F_x^M, F_y^M, F_z^M) match closely with the directly measured forces, and the residual terms ($F_x^{\text{res}}, F_y^{\text{res}}, F_z^{\text{res}}$) remain within ± 0.4 N, demonstrating excellent calibration alignment between the force and moment bridges. The measured normal forces correlate linearly with the penetration depths computed from the wall constraint model, yielding correlation coefficients $R^2 > 0.97$. Moment magnitudes were below 0.3 N m, indicating negligible off-axis or torsional loads—a desirable condition for pHRI safety.

5.10. Passivity, Z-width adaptation, and energy analysis

The stability of the pHRI interaction is verified by the environment power and energy metrics. The instantaneous power $P_{\text{env}} = -\mathbf{F}_{\text{wall}}^\top \mathbf{v}$ fluctuates around zero, indicating that the environment (virtual wall) does not inject net energy into the system. The accumulated tank energy E_{env} remains bounded throughout the experiment, with short transients when contact is first established and released. During repeated wall impacts, E_{env} never exceeded the imposed threshold, remaining well within the admissible limit for stable operation set by E_{th} . The corresponding K_w dropped rapidly from its initial value and recovered smoothly after contact release, consistent with the decay factor $\eta_\downarrow = 0.5$ and the recovery rate $r_\uparrow = 0.010$. Such automatic regulation enhances user safety and transparency without perceivable delay or stiffness oscillation.

5.11. Discussion

The combined results validate the efficacy of the proposed pHRI control scheme. The Delta robot equipped with the custom six-axis F/T sensor exhibited smooth, stable, and energetically passive interaction during both free-space and constrained tasks. The admittance framework successfully

rendered compliant behavior that was natural to the human operator, while the passivity observer and Z-width adaptation maintained energetic consistency even under abrupt contact transitions. The measured force–position relations align closely with theoretical predictions, confirming accurate force sensing and effective decoupling of dynamics among the translational axes.

Future improvements include extending the control law to multi-surface constraint handling, online identification of human hand impedance parameters, and integration of the neural estimator introduced in Section 3 for real-time stiffness estimation. The current experimental findings provide a strong foundation for subsequent studies on cooperative manipulation and human-intent inference using the Delta-type pHRI platform.

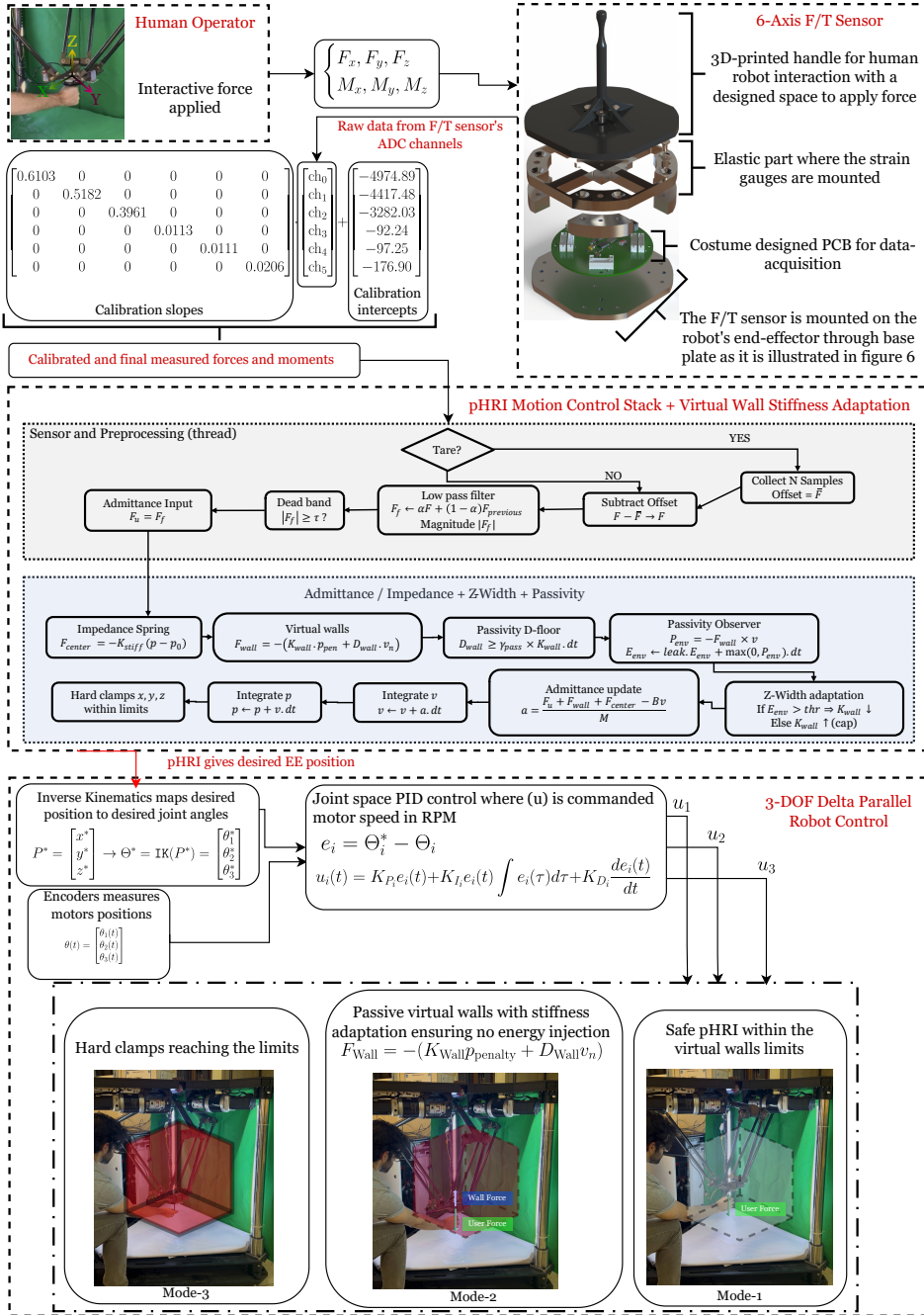


Figure 7: Overview of the experimental pHRI pipeline. Human-applied forces are measured by the embedded six-axis F/T sensor, preprocessed on the host PC, and passed to an admittance controller incorporating virtual walls, passivity enforcement, and Z-width stiffness adaptation. The resulting Cartesian commands are executed by the 3-DOF Delta robot.

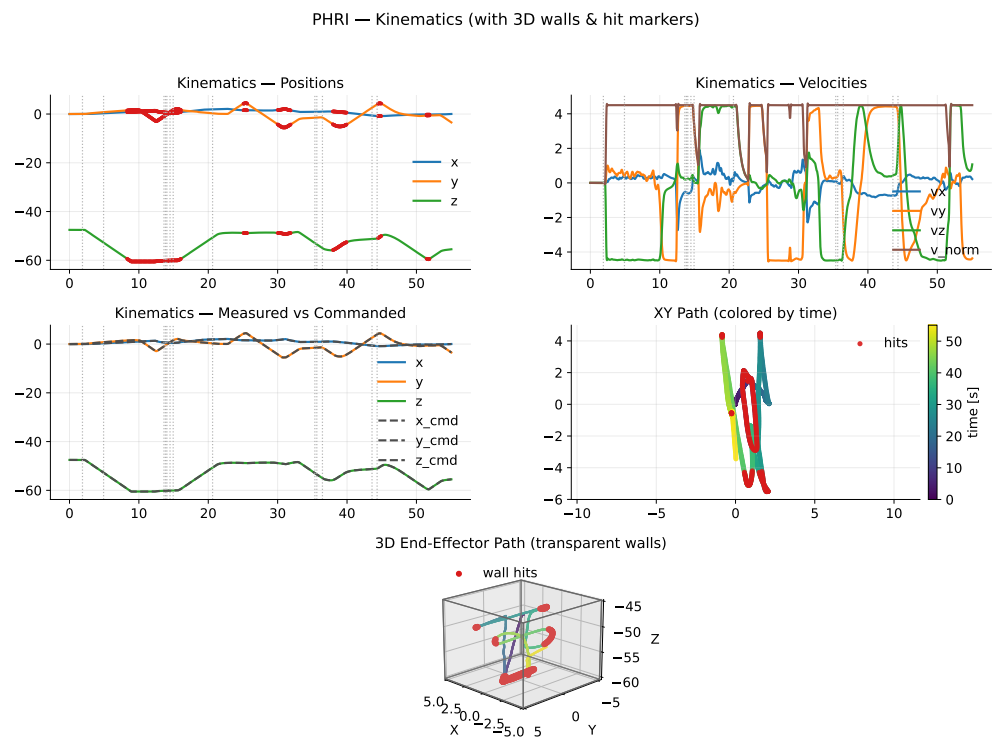


Figure 8: End-effector kinematic responses during the pHRI task. Cartesian position and velocity profiles, 3D trajectory with transparent virtual walls and contact markers, and commanded versus measured motion along each axis.

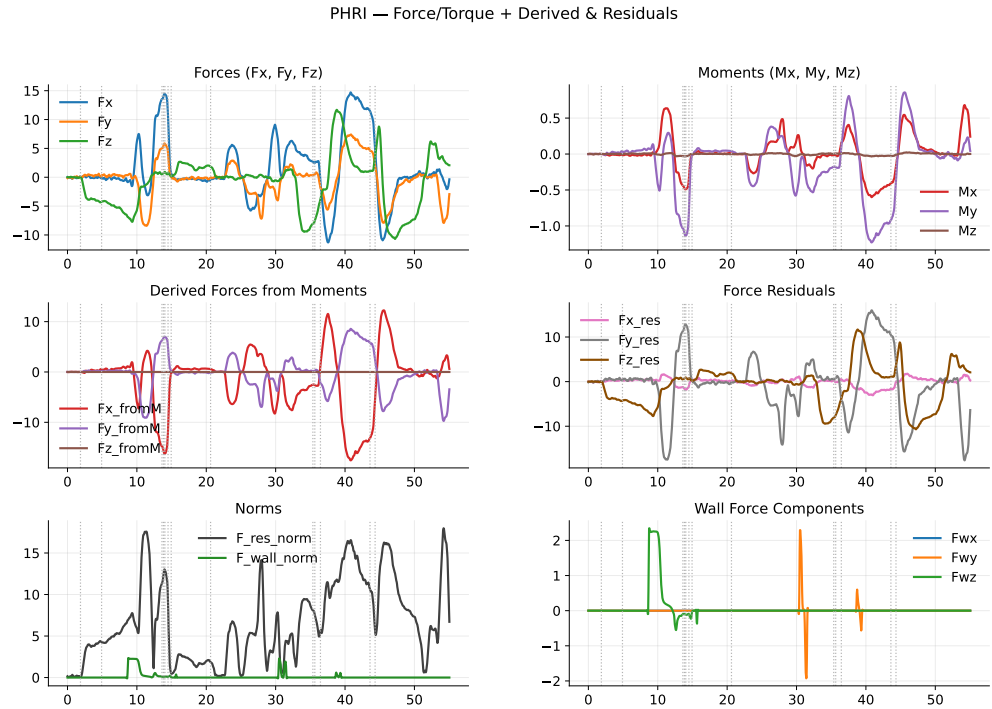


Figure 9: Measured and derived force–moment signals during interaction. (a) Cartesian force components (F_x, F_y, F_z); (b) moment components (M_x, M_y, M_z) used for safety monitoring; (c) forces reconstructed from moments and residual differences.

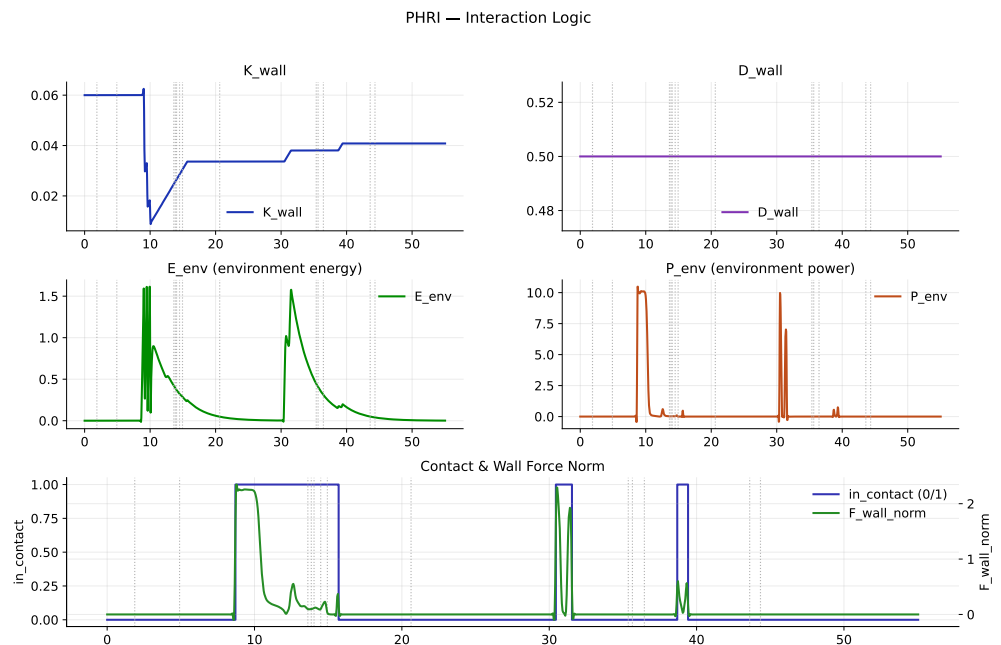


Figure 10: Passivity and stiffness adaptation results during interaction. (a) Wall force components and total contact force magnitude; (b) evolution of virtual wall stiffness K_w and damping D_w during contact; (c) environment power P_{env} and accumulated energy E_{env} with in-contact intervals.

6. Conclusion

We presented a six-axis strain-gauge force/torque sensor purpose-built for pHRI together with a practical calibration methodology. The transducer combines a cruciform elastic body with six full-bridge networks and a custom four-layer PCB featuring a 24-bit ADC and embedded synchronization. The low-cost calibration rig applies decoupled loads across all axes and enables linear least-squares fitting of a diagonal calibration map. Experiments report nonlinearity below 0.39%FS, repeatability better than 0.38%FS, accuracy above 99.4% on all axes, and resolutions of 0.47 N (force) and 0.015 N m (torque) at the 99% criterion. A pHRI case study on a Delta robot validated admittance control with virtual fixtures and demonstrated passivity-preserving Z-width adaptation that automatically reduces wall stiffness during energetic transients and recovers it afterward. The presented sensor and control stack offer a practical, reproducible foundation for safe, intuitive human–robot collaboration.

References

- [1] V. Kamble, V. shinde, J. Kittur, R. Scholar, Profesoor, Overview of load cells (10 2021).
- [2] T. A. Dwarakanath, D. Venkatesh, Simply supported, ‘Joint less’ parallel mechanism based force–torque sensor, *Mechatronics* 16 (9) (2006) 565–575. doi:10.1016/j.mechatronics.2006.03.013.
- [3] Z. Zhang, Y. Chen, D. Zhang, J. Xie, M. Liu, A six-dimensional traction force sensor used for human-robot collaboration, *Mechatronics* 57 (2019) 164–172. doi:10.1016/j.mechatronics.2018.12.005.
- [4] J. Yao, D. Cai, H. Zhang, H. Wang, D. Wu, Y. Zhao, Task-oriented design method and research on force compliant experiment of six-axis wrist force sensor, *Mechatronics* 35 (2016) 109–121. doi:10.1016/j.mechatronics.2016.01.007.
- [5] D. Chen, A. Song, A. Li, Design and calibration of a six-axis force/torque sensor with large measurement range used for the space manipulator, *Procedia Engineering* 99 (2015) 1164–1170, 2014 Asia-Pacific International Symposium on Aerospace Technology (APISAT2014), September 24–26, 2014, Shanghai, China.
- [6] G. Boschetti, R. Caracciolo, D. Richiedei, A. Trevisani, Model-based dynamic compensation of load cell response in weighing machines affected by environmental vibrations, *Mechanical Systems and Signal Processing* 34 (1) (2013) 116–130.
- [7] W. Y. Kim, S. Y. Ko, J.-O. Park, S. Park, 6-dof force feedback control of robot-assisted bone fracture reduction system using double f/t sensors and adjustable admittances to protect bones against damage, *Mechatronics* 35 (2016) 136–147. doi:10.1016/j.mechatronics.2016.02.005.
- [8] T. Li, J. Guo, H. Zheng, S. Wang, L. Qiu, H. Ren, Fault-tolerant six-axis fbg force/moment sensing for robotic interventions, *IEEE/ASME Transactions on Mechatronics* 28 (6) (2023) 3537–3550. doi:10.1109/TMECH.2023.3268077.
- [9] A. Srivastava, R. Xu, A. Escoto, C. Ward, R. Patel, Design of an ultra thin strain sensor using superelastic nitinol for applications in

- minimally invasive surgery, in: 2016 IEEE/ASME International Conference on Advanced Intelligent Mechatronics (AIM), 2016, pp. 794–799. doi:10.1109/AIM.2016.7576865.
- [10] R. Cortesão, M. Dominici, Robot force control on a beating heart, *IEEE/ASME Transactions on Mechatronics* 22 (4) (2017) 1736–1743. doi:10.1109/TMECH.2017.2696259.
 - [11] Y. C. Kim, Y. S. Ihn, H. R. Choi, S. M. Lee, J. C. Koo, Implementation of force sensor with multi strain gauges for enhancing accuracy and precision, in: Proceedings of the 2010 IEEE/ASME International Conference on Mechatronic and Embedded Systems and Applications (MESA), 2010, pp. 192–195. doi:10.1109/MESA.2010.5552076.
 - [12] U. Kim, D.-H. Lee, Y. B. Kim, D.-Y. Seok, H. R. Choi, A novel six-axis force/torque sensor for robotic applications, *IEEE/ASME Transactions on Mechatronics* 22 (3) (2017) 1381–1391. doi:10.1109/TMECH.2016.2640194.
 - [13] J.-K. Min, K.-H. Ahn, H.-C. Park, J.-B. Song, A novel reactive-type joint torque sensor with high torsional stiffness for robot applications, *Mechatronics* 63 (2019) 102265. doi:10.1016/j.mechatronics.2019.102265.
 - [14] R. Ranganath, P. S. Nair, T. S. Mruthyunjaya, A. Ghosal, A force-torque sensor based on a stewart platform in a near-singular configuration, *Mechanism and Machine Theory* 39 (9) (2004) 971–998. doi:10.1016/j.mechmachtheory.2004.04.005.
 - [15] Z. Wang, J. Yao, Y. Xu, Y. Zhao, Hyperstatic analysis of a fully pre-stressed six-axis force/torque sensor, *Mechanism and Machine Theory* 57 (2012) 84–94. doi:10.1016/j.mechmachtheory.2011.10.016.
 - [16] Y. Lu, L. Chen, P. Wang, B. Zhang, Statics and stiffness analysis of a novel six-component force/torque sensor with a 3-rpps compliant parallel structure, *Mechanism and Machine Theory* 62 (2013) 99–111. doi:10.1016/j.mechmachtheory.2012.11.011.
 - [17] Z. Li, H. Wei, H. Zhang, C. Liu, A variable admittance control strategy for stable and compliant human-robot physical interaction, *IEEE Robotics and Automation Letters* 10 (2) (2025) 1138–1145. doi:10.1109/LRA.2024.3519885.

- [18] J. Dong, J. Xu, Q. Zhou, S. Hu, Physical human–robot interaction force control method based on adaptive variable impedance, *Journal of the Franklin Institute* 357 (12) (2020) 7864–7878.
- [19] M. Sharifzadeh, M. T. Masouleh, A. Kalhor, On human–robot interaction of a 3-dof decoupled parallel mechanism based on the design and construction of a novel and low-cost 3-dof force sensor, *Meccanica* 52 (10) (2016) 2471–2489.
- [20] A. D. Santis, A. Albu-Schäffer, A. D. Luca, B. Siciliano, An atlas of physical human–robot interaction, *Mechanism and Machine Theory* 43 (3) (2008) 253–270. doi:10.1016/j.mechmachtheory.2007.03.006.
- [21] Z. Du, Y. Liang, L. Zhang, B. Chen, et al., Human-robot interaction control of a haptic master manipulator used in laparoscopic minimally invasive surgical robot system, *Mechanism and Machine Theory* 156 (2021) 103958. doi:10.1016/j.mechmachtheory.2020.103958.
- [22] F. J. Ruiz-Ruiz, J. Ventura, C. Urdiales, J. M. G. de Gabriel, Compliant gripper with force estimation for physical human–robot interaction, *Mechanism and Machine Theory* 178 (2022) 105062. doi:10.1016/j.mechmachtheory.2022.105062.
- [23] Z. Wang, G. C. Liu, S. Qian, D. Wang, X. Wei, X. Yu, et al., Tracking control with external force self-sensing ability based on position/force estimators and non-linear hysteresis compensation for a backdrivable cable-pulley-driven surgical robotic manipulator, *Mechanism and Machine Theory* 183 (2023) 105259. doi:10.1016/j.mechmachtheory.2023.105259.
- [24] C. G. Kang, Performance improvement of a 6-axis force-torque sensor via novel electronics and cross-shaped double-hole structure, *International Journal of Control, Automation and Systems* 3 (2005) N/A.
- [25] A. Ehsani, N. Khomami, M. Ghaneie, M. Masouleh, Design and fabrication of an optimized six-axis force-torque sensor, in: Proceedings of 2023 IEEE International Conference on Robotics and Mechatronics (ICRoM), 2023, pp. 598–605. doi:10.1109/ICRoM60803.2023.10412501.
- [26] F. Ballo, M. Gobbi, G. Mastinu, G. Previati, A six axis load cell for the analysis of the dynamic impact response of a hybrid iii dummy, *Measurement* 90 (2016) N/A. doi:10.1016/j.measurement.2016.04.047.

- [27] Y. Haddab, Q. Chen, P. Lutz, Improvement of strain gauges micro-forces measurement using kalman optimal filtering, *Mechatronics* 19 (4) (2009) 457–462. doi:10.1016/j.mechatronics.2008.11.012.
- [28] B. Denkena, J. Kiesner, Strain gauge based sensing hydraulic fixtures, *Mechatronics* 34 (2016) 111–118. doi:10.1016/j.mechatronics.2015.05.008.
- [29] J. O. Templeman, O. Sheil, M. D. Gilchrist, A. A. S. Gillies, Multi-axis force sensors: A state-of-the-art review, *Sensors and Actuators A: Physical* 306 (2020) 111971.
- [30] V. Grosu, S. Grosu, B. Vanderborght, D. Lefeber, C. Rodriguez-Guerrero, Multi-axis force sensor for human–robot interaction sensing in a rehabilitation robotic device, *Sensors* 17 (6) (2017) 1294. doi:10.3390/s17061294.
- [31] S. Traversaro, D. Pucci, F. Nori, et al., Model based in situ calibration of six axis force torque sensors, arXiv:1610.03305 (2016).
- [32] F. J. A. Chavez, S. Traversaro, D. Pucci, F. Nori, Six-axis force torque sensor model-based in situ calibration with temperature compensation, *Sensors* 19 (24) (2019) 5521. doi:10.3390/s19245521.
- [33] J. Zhenlin, G. Feng, Z. Xiaohui, Design and analysis of a novel isotropic six-component force/torque sensor, *Sensors and Actuators A: Physical* 109 (1–2) (2003) 17–20. doi:10.1016/S0924-4247(03)00299-1.
- [34] Q. Liang, D. Zhang, Q. Song, Y. Ge, H. Cao, Y. Zhu, Design and fabrication of a six-dimensional wrist force/torque sensor based on e-type membranes compared to cross beams, *Measurement* 43 (10) (2010) 1702–1715. doi:10.1016/j.measurement.2010.07.019.
- [35] M. Guibert, V. Grosu, C. Duriez, A versatile flexure-based 6-axes force/torque sensor, arXiv:2106.08210 (2021).
- [36] J. Kim, D. Lee, Y. Kim, et al., A compact six-axis force/torque sensor using inductive resonance measurement, *Review of Scientific Instruments* 95 (8) (2024) 085006. doi:10.1063/5.0214189.
- [37] C.-Y. Lin, A. R. Ahmad, G. A. Kebede, Novel mechanically fully decoupled six-axis force-moment sensor, *Sensors* 20 (2) (2020) 395. doi:10.3390/s20020395.

- [38] A. Valizadeh, A. Akbarzadeh, M. H. Tashakori Heravi, Effect of structural design parameters of a six-axis force/torque sensor using full factorial design, in: Proc. 3rd RSI Int. Conf. Robotics and Mechatronics (ICRoM), 2015, pp. 789–793.
- [39] L. Fu, A. Song, Dynamic characteristics analysis of the six-axis force/torque sensor, Journal of Sensors (2018) 1–11.